Evolution of possible Weyl semimetal states across the Mott transition in pyrochlore iridates induced by hole doping

K. Ueda,[1] H. Fukuda,[1] R. Kaneko,[1,2] J. Fujioka,[3] and Y. Tokura[1,2,4]
[1]*Department of Applied Physics, University of Tokyo, Tokyo 113-8656, Japan*
[2]*RIKEN Center for Emergent Matter Science, Wako 351-0198, Japan*
[3]*Faculty of Material Sciences, University of Tsukuba, Tsukuba 305-8577, Japan*
[4]*Tokyo College, University of Tokyo, Tokyo 113-8656, Japan*

(Received 18 September 2020; revised 28 November 2020; accepted 4 December 2020; published 21 December 2020)

We study possible Weyl semimetals of strongly correlated electrons by investigating magnetotransport properties in pyrochlore $R_2Ir_2O_7$ (R denotes rare-earth ions), choosing three types of R ions to design the exchange coupling scheme between R $4f$ and Ir $5d$ moments: nonmagnetic Eu ($4f^6$), isotropic Gd ($4f^7$), and anisotropic Tb ($4f^8$). In the doping-induced semimetallic state, distinctive features of magnetoresistance and the Hall effect are observed in R = Gd and Tb compounds due to the effects of the exchange-enhanced isotropic and anisotropic Zeeman fields, respectively, exemplifying the double-Weyl semimetal and the two-in two-out line-node semimetal as predicted by theories. In particular, the Hall angle of an R = Gd compound is strongly enhanced to 1.5% just above the critical doping for the Mott transition. Furthermore, an unconventional Hall contribution is discerned for a lower doping regime of the R = Gd compound, which can be ascribed to the emergence of Weyl points with the field-distorted all-in all-out order state. These findings indicate that the hole-doping-induced Mott transition as well as the characteristic f-d exchange interaction stabilizes versatile topological semimetal states in a wide range of material parameter space.

DOI: 10.1103/PhysRevB.102.245131

I. INTRODUCTION

The correlation between magnetism and topological electronic states has been one of the most important themes of the modern condensed matter physics [1,2]. A magnetic Weyl semimetal (WSM) possesses crossings of nondegenerate bands with linear dispersion under the breaking of time-reversal symmetry with magnetic order [3]. Notably, the crossing (Weyl point) can be viewed as a magnetic monopole of Berry curvature in the momentum space, proven to yield salient magnetotransport properties [4]. A prominent example is the intrinsic anomalous Hall effect (AHE) [5]. Recent extensive studies on this subject reveal that the position of Weyl points relative to the Fermi energy E_F is intimately related to the size of the AHE, revealing an astoundingly large AHE in a variety of magnets [6–9]. Despite such remarkable findings, the role of electron correlation as a source of magnetism in topological electronic states remains elusive. In particular, the emergence of the magnetic topological states over the electron-correlation-induced metal-insulator transition (MIT) [10] has seldom been explored.

Pyrochlore oxide $A_2B_2O_7$ is known to host exotic quantum magnetic ground states [11] and was recently proposed to host topological electronic states for iridium oxides $R_2Ir_2O_7$ (R being rare-earth or Y ions) [3]. The merit of pyrochlore oxides is that the effective electron correlation U/W and the band filling n (=1 − δ, δ being hole doping) can be tuned by varying A-site ions in a similar manner to perovskites [10]. For instance, $R_2Ir_2O_7$ with a smaller ionic size R shows an effectively larger bending of the Ir-O-Ir bond angle and hence leads to a smaller one-electron bandwidth W; thus the R-ion size is a good indicator of the inverse of the effective electron correlation U/W, as shown in Fig. 1(a). Among a variety of $R_2Ir_2O_7$, the R = Pr compound, which is characterized by the largest R ionic radius, is found to possess a quadratic band touching (QBT) of spin degenerate valence and conduction bands near E_F in the paramagnetic metal (PM) phase [see Fig. 1(b)] [12]. Since the QBT is protected by the cubic crystalline symmetry and the time-reversal symmetry, it is expected to be robust against the perturbation as long as the symmetry is kept intact. Such an electronic state is termed a Luttinger semimetal (SM) or QBT SM that is theoretically anticipated to be converted to versatile topological states by symmetry-breaking procedures [13,14]. Figure 1(b) displays a schematic picture of the electronic band modulation across Mott transitions. The strong Hubbard repulsion U brings about the antiferromagnetiklike all-in all-out (AIAO) type of magnetic order [depicted in the inset in Fig. 1(a)] and lifts the band degeneracy of QBT, leading to the emergence of WPs along the high-symmetry axes [1,15], termed AIAO WSM hereafter. Although WSM is generally robust against the perturbation, WPs in this system migrate towards the Brillouin zone boundary with increasing U/W or the magnetic order parameter m. Consequently, with a tiny increase of U or m, WSM undergoes the pair annihilation of WPs at the zone boundary and turns into a gapped insulating state [Fig. 1(b)], hampering the observation in the momentum space. In spite of such difficulty, intensive studies on R = Nd and Pr compounds have unveiled a

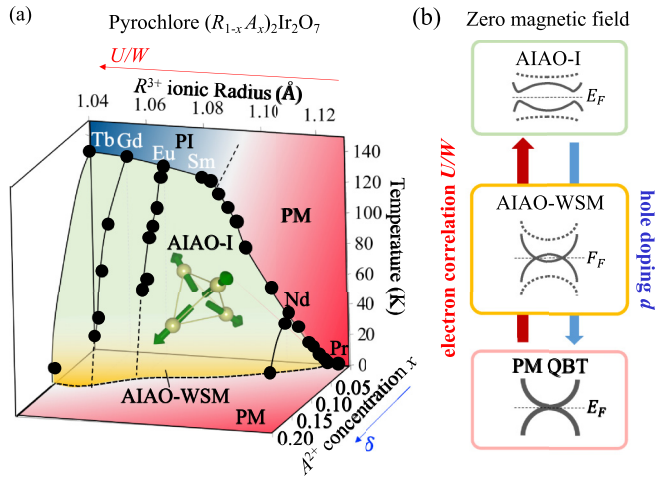

FIG. 1. (a) Phase diagram of $R_2Ir_2O_7$ as a function of rare-earth ionic radius, divalent-ion concentration, and temperature. Here PI stands for paramagnetic insulator, PM stands for paramagnetic metal, AIAO stands for all-in all-out state, and WSM stands for Weyl semimetal. (b) Schematic picture of modulation of electronic band structures as a function of electron correlation U and hole doping δ. Here QBT stands for quadratic band touching.

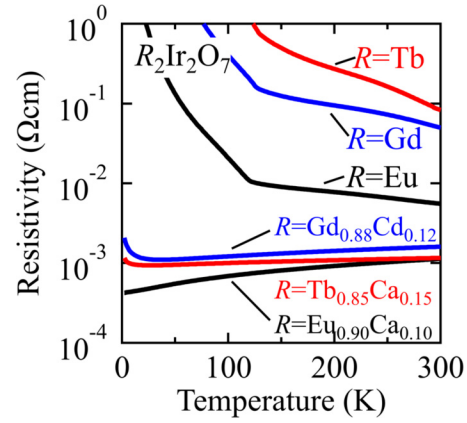

FIG. 2. Temperature dependence of resistivity for $(Eu_{1-x}Ca_x)_2Ir_2O_7$ ($x = 0$ and 0.10), $(Gd_{1-x}Cd_x)_2Ir_2O_7$ ($x = 0$ and 0.12), and $(Tb_{1-x}Ca_x)_2Ir_2O_7$ ($x = 0$ and 0.15).

number of emergent transport phenomena such as an unusual Hall effect [16,17], magnetic-field-induced MITs [18–20], and anomalous metallic states on the magnetic domain walls in the AIAO state [21,22], which are all understood in the context of underling or incipient WSM states induced by the time-reversal symmetry breaking (Fig. 7 in the Appendix).

On the other hand, $R_2Ir_2O_7$ compounds with smaller R ionic radius are not QBT SM but fully gapped insulators because of larger U/W [Fig. 1(a)] and thus have been considered to be no longer related to topological semimetallic state [23]. However, recent studies demonstrate that the hole doping by the chemical substitution of trivalent R ions with divalent A ions turns them into a PM state [24–27] in which, remarkably, QBT SM can ubiquitously subsist even if the chemical substitution introduces some disorders [25]. In this sense, the hole-doped $R_2Ir_2O_7$ offers a fertile playground to study the correlation between magnetism and topological electronic states, since carrier doping can tune the position of the QBT node with respect to E_F and moreover a variety of local R $4f$ magnetic spins, which strongly affect itinerant Ir $5d$ electrons through the f-d coupling, are available in this pyrochlore system.

II. RESULTS

A. Hole-doping-induced insulator-metal transition

In this work we choose three R ions to study the role of R magnetic moment in the magnetic-field-induced modification of the QBT state: nonmagnetic $R =$ Eu ($4f^6$), isotropic $R =$ Gd ($4f^7$), and Ising-type $R =$ Tb ($4f^8$). We synthesize high-quality polycrystals by utilizing high-pressure apparatus which promotes the pyrochlore-lattice formation while keeping the right stoichiometry of compounds. Employing the growth condition described elsewhere [28], we obtain the hard and dense samples suitable for the systematic transport measurements. As for the chemical substitution of trivalent R ions with divalent A ions, we find that $A =$ Ca (Cd) is suitable for $R =$ Eu and Tb (Gd) in the light of the ion-size matching. This allows us to examine the hole-doping effect while suppressing other contributions such as the A-site doping-induced change of bandwidth or disorder. Zhu *et al.* demonstrated that the Ca doping to $Y_2Ir_2O_7$ enhances both metallicity and ferromagnetism [26]. They found that the temperature dependence of resistivity shows a minimum at around 100 K for the heavily doped metallic sample, which is somewhat different from our result as shown below. We speculate that it is due to the mismatch of A-site ionic radii. Since the Ca ionic radius is much larger than that of Y ions, the Ca doping modifies the effective bandwidth via the change of Ir-O-Ir bond angles and thereby brings about the resistivity minimum at around 100 K, which is also observed in $Eu_2Ir_2O_7$ under a hydrostatic pressure above 7.88 GPa [29].

As the A^{2+} concentration x increases in $(Gd_{1-x}Cd_x)_2Ir_2O_7$ and $(Tb_{1-x}Ca_x)_2Ir_2O_7$, which corresponds to the nominal hole doping δ, both exhibit a systematic reduction in resistivity ρ_{xx} as well as in T_N that shows up as a kink of ρ_{xx} in accord with the anomaly in M. They turn into PM at sufficiently large x, although the resistivity slightly increases below 20 K as shown in Fig. 2. The results including T_N are summarized in the phase diagram in Fig. 1(a). Incidentally, the upturn of ρ_{xx} at low temperatures in $(Tb_{1-x}Ca_x)_2Ir_2O_7$ and $(Gd_{1-x}Cd_x)_2Ir_2O_7$, which is absent in $(Eu_{1-x}Ca_x)_2Ir_2O_7$, is due perhaps to the strong magnetic coupling between itinerant Ir electrons and localized R moments which produces incoherent carrier-electron scattering [30,31]. Since the ρ_{xx} value of $(Eu_{0.90}Ca_{0.10})_2Ir_2O_7$ is close to those of $(Gd_{0.88}Cd_{0.12})_2Ir_2O_7$ and $(Tb_{0.85}Ca_{0.15})_2Ir_2O_7$, realization of similar electronic states that host QBT at the Γ point is anticipated in hole-doped analogs of both $R =$ Gd and Tb compounds, which is corroborated by magnetotransport measurements described in the following.

B. Magnetotransport of metallic *R* compounds

Having thus realized the QBT state in various magnetic $(R_{1-x}A_x)_2Ir_2O_7$ compounds, we study the magnetic-field de-

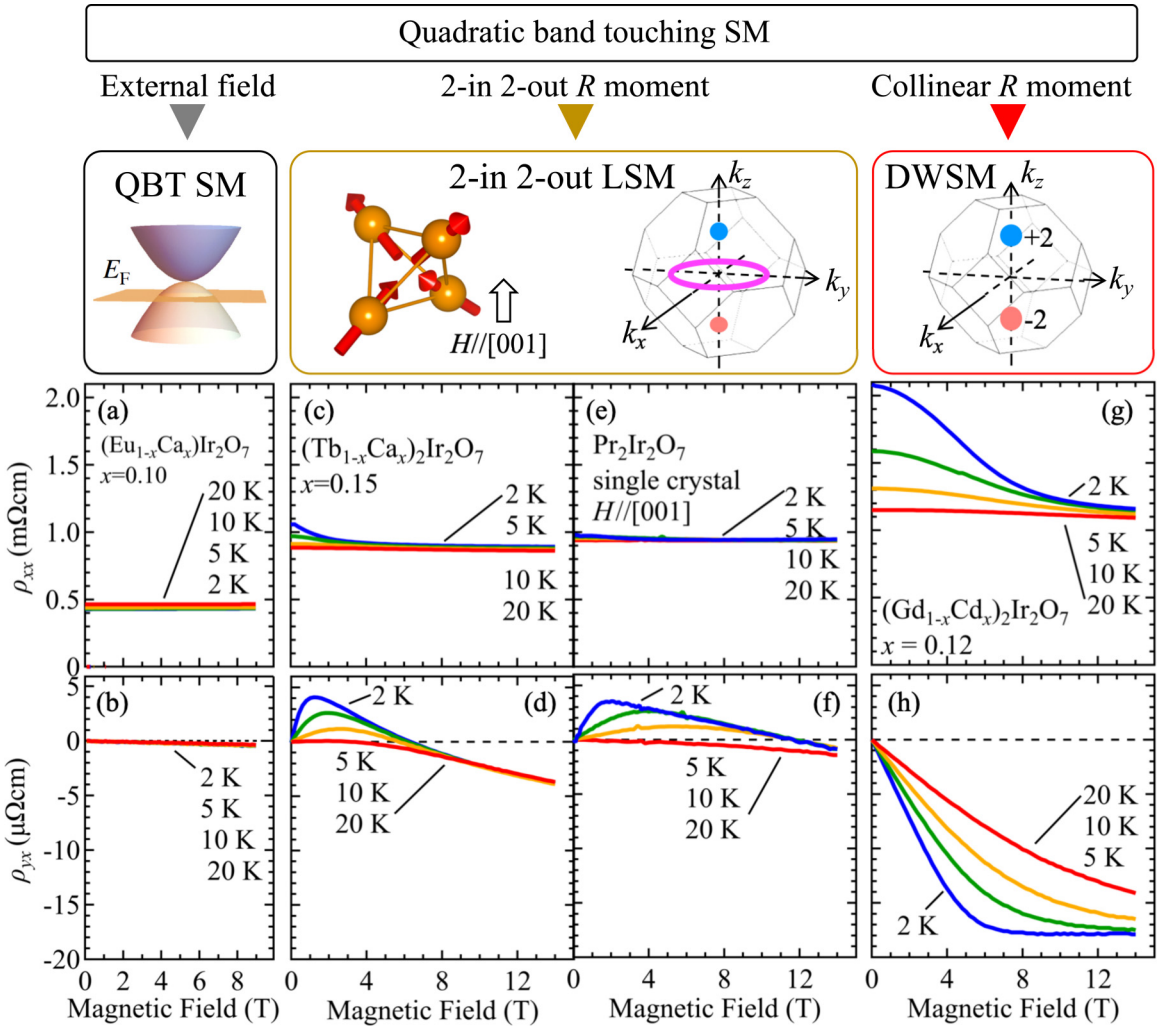

FIG. 3. Magnetic-field dependence of (a), (c), (e), and (g) longitudinal resistivity and (b), (d), (f), and (h) Hall resistivity for (a) and (b) $(Eu_{1-x}Ca_x)_2Ir_2O_7$ ($x = 0.10$), (c) and (d) $(Tb_{1-x}Ca_x)_2Ir_2O_7$ ($x = 0.15$), (e) and (f) $Pr_2Ir_2O_7$, and (g) and (h) $(Gd_{1-x}Cd_x)_2Ir_2O_7$ ($x = 0.12$). Schematic magnetic configurations of R spins and expected electronic structures are displayed on top of the respective windows.

pendence of ρ_{xx} and Hall resistivity ρ_{yx} in Fig. 3. The $(Eu_{0.90}Ca_{0.10})_2Ir_2O_7$ compound, whose R-site ion is nonmagnetic, shows little magnetic-field dependence of ρ_{xx} [Fig. 3(a)] and ρ_{yx} apart from the normal Hall effect [Fig. 3(b)]. On the other hand, negative magnetoresistance is clearly observed for $(Tb_{1-x}Ca_x)_2Ir_2O_7$ with $x = 0.15$ in Fig. 3(c), indicating the coupling between the conduction electron and R-ion moment. More importantly, ρ_{yx} shows a complicated magnetic-field profile especially at 2 K [Fig. 3(d)]; as the field increases, ρ_{yx} abruptly increases with a maximum around 1 T and subsequently plunges to the negative value, changing the sign at 7 T. To identify the origin of nonmonotonic Hall responses for $(Tb_{1-x}Ca_x)_2Ir_2O_7$, we examine those of well-oriented single-crystal $Pr_2Ir_2O_7$, which is well characterized by the QBT SM state at zero field and zero doping ($\delta = 0$) [12] and by an Ising anisotropy of R moment similar to the Tb one. Figures 3(e) and 3(f) display ρ_{xx} and ρ_{yx} of $Pr_2Ir_2O_7$ (single crystal), respectively, as a function of the magnetic field along the [001] axis which favors a two-in two-out state as depicted on top of Figs. 3(c) and 3(e). Both ρ_{xx} and ρ_{yx} are qualitatively similar to those of $(Tb_{1-x}Ca_x)_2Ir_2O_7$ ($x = 0.15$). A former study combining transport measurements on $(Nd, Pr)_2Ir_2O_7$ and theoretical calculation suggests that the magnetic field can modulate the electronic state into the line-node SM (LSM) depicted in the middle panel of Fig. 2 via the magnetic stabilization at the two-in two-out state [18]. Thus, the close similarity of ρ_{xx} and ρ_{yx} in the two compounds with similar Ising anisotropy of R moments implies that the LSM can be also realized in $(Tb_{1-x}Ca_x)_2Ir_2O_7$ polycrystals at high fields where the two-in two-out configuration is dominant.

On the other hand, a very different trend of ρ_{xx} and ρ_{yx} is observed in $(Gd_{1-x}Cd_x)_2Ir_2O_7$ ($x = 0.12$). In particular, at the lowest temperature 2 K, ρ_{xx} markedly decreases by half at 14 T [Fig. 3(g)] while the absolute value of negative ρ_{yx} increases rapidly. This anomalous Hall-like behavior in the originally paramagnetic but field-magnetized state can show the large ρ_{yx} value, 20 times larger than that of the $R = Eu$ compound [Fig. 3(h)], and the observed value of the Hall angle is as large as 1.5%. For instance, the Hall angle of ferromagnetic oxides such as $SrRuO_3$ [32] and $(La, Sr)CoO_3$ [33]

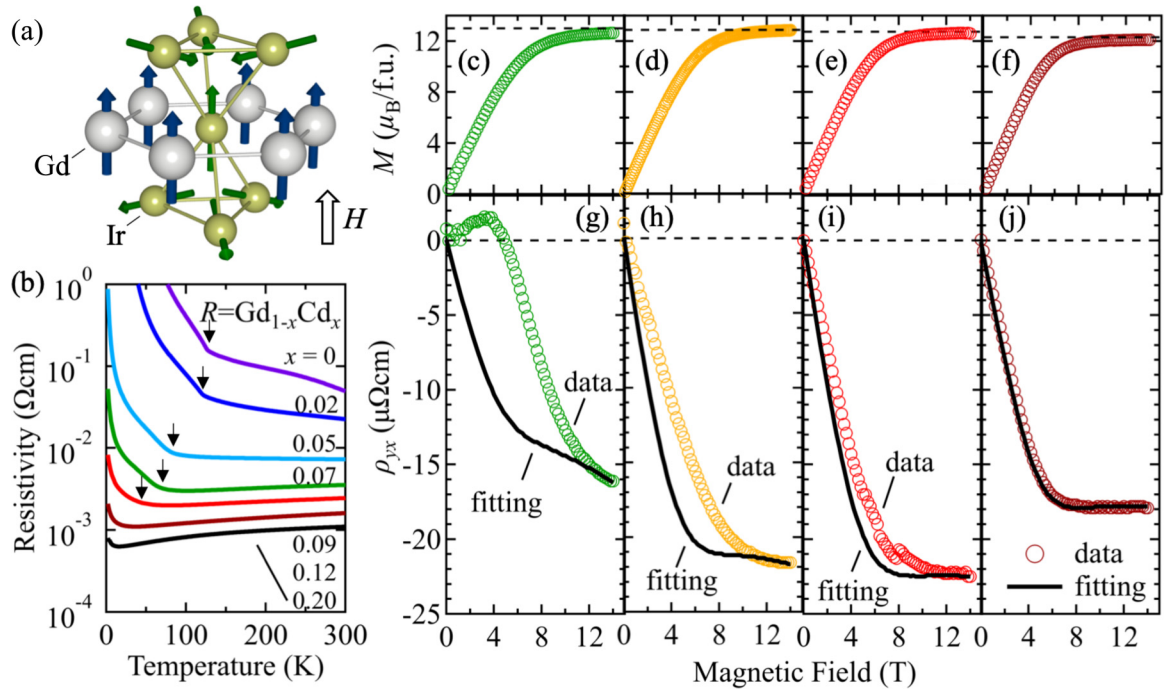

FIG. 4. (a) Schematic magnetic structures of Ir moments (green) and Gd moments (blue). (b) Temperature dependence of resistivity for $(Gd_{1-x}Cd_x)_2Ir_2O_7$ with various x. Arrows indicate the magnetic transition temperature. Also shown is the magnetic-field dependence H of (c)–(f) magnetization M and (g)–(j) Hall resistivity at 2 K in $(Gd_{1-x}Cd_x)_2Ir_2O_7$ for (c) and (g) $x = 0.07$, (d) and (h) $x = 0.08$, (e) and (i) $x = 0.09$, and (f) and (j) $x = 0.12$. Thick black lines are fitting curves with the H-linear normal Hall plus the M-linear anomalous Hall terms (see the text).

is approximately 0.9% and that of the isostructural ferromagnet $Nd_2Mo_2O_7$ with the two-in two-out scalar spin chirality is about 1.3% [34]. Such a large Hall effect can point to a substantial Berry-curvature contribution near E_F in the momentum space. Oh *et al.* showed theoretically that the uniform magnetic field along the [001] crystalline direction lifts the band degeneracy into two Weyl points hosting the monopole charge ±2 on the [001] momentum axis, as depicted on top of Fig. 3(g) (and in Fig. 7 in the Appendix) [35]. It is termed double-Weyl semimetal (DWSM). Apparently, this situation cannot be caused by a simple external-field-induced Zeeman splitting; if so, the R = Eu compound would show a similar effect, but not in reality [Fig. 3(b)]. The sufficiently large exchange splitting of QBT is only driven by the f-d exchange coupling from six nearest-neighbor Gd spins which are easily aligned by external fields [Fig. 4(a)].

C. Magnetotransport across the filling-control-induced metal-insulator transition in $(Gd_{1-x}Cd_x)_2Ir_2O_7$

In order to gain deeper insight into the possible topological-state change in $(Gd_{1-x}Cd_x)_2Ir_2O_7$, we implement a precise investigation of magnetotransport properties across a doping-induced Mott transition. Figure 4(b) shows the temperature dependence of ρ_{xx} for several $(Gd_{1-x}Cd_x)_2Ir_2O_7$ compounds with varying x. Accompanied by the decline of ρ_{xx}, T_N, which is indicated by arrows in Fig. 4(b), is gradually suppressed with increasing x and no longer discernible for $x > 0.10$. The temperature dependence of M for several x is displayed in Fig. 8 in the Appendix. At $x = 0.07$, M in the field-cooling process clearly deviates from that in the zero-field-cooling process below T_N at which ρ_{xx} shows a kink. The deviation disappears down to 2 K for $x = 0.12$, although the upturn of ρ_{xx} subsists. The upturn of ρ_{xx} is also observed in Ca-doped $Nd_2Ir_2O_7$ below 20 K [27] and is attributed to the ordering or freezing of the Nd magnetic sublattice which is observed by muon spin resonance [36]. Figures 4(c)–4(j) show the magnetic-field dependence of M and ρ_{yx} at 2 K for various compositions near the Mott transition, ranging from the $x = 0.07$ compound, which undergoes long-range AIAO order below T_N, to the paramagnetic semimetal $x = 0.12$ compound. As shown in Figs. 4(c)–4(f), M increases monotonically with increasing field and finally saturates at high fields for all compositions. The saturated M values are consistent with those expected from fully aligned Gd spins as depicted by dashed lines. The critical magnetic field, which is required to reach the saturated M, gradually becomes smaller as x increases; it is roughly 11 T for $x = 0.07$ and 8 T for $x = 0.12$. This is presumably because the AIAO-type antiferromagnetic correlation of Ir moments in the small-x region competes with the collinear alignment of Gd moments via the f-d coupling. Figures 4(g)–4(j) display ρ_{yx} at 2 K as a function of the magnetic field. Interestingly, ρ_{yx} for $x = 0.07$ shows a nonmonotonic field dependence that is explicitly distinguished from the usual AHE [Fig. 4(g)]. As the field increases, ρ_{yx} increases with a broad maximum around 3 T and then markedly decreases with the sign reversal. Finally, ρ_{yx} decreases modestly above 11 T at which point M is saturated. This characteristic field dependence at 2 K fades out into the monotonic change as the temperature is elevated (see Fig. 9

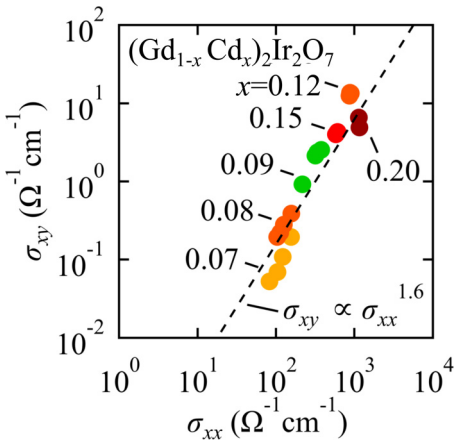

FIG. 5. A log-log plot of Hall conductivity versus longitudinal conductivity for $(Gd_{1-x}Cd_x)_2Ir_2O_7$ with various x. The dashed line indicates the relation $\sigma_{xy} \propto \sigma_{xx}^{1.6}$.

in the Appendix). On the other hand, ρ_{yx} for $x = 0.12$ monotonically decreases and saturates at around 8 T, seemingly in proportion to M [Fig. 4(j)].

To understand this behavior, we employ the fitting function which is conventionally used for ferromagnets, expressed as $\rho_{yx}^{\text{fit}} = R_0 B + \mu_0 R_s M$, where R_0 is the normal Hall coefficient and R_s is the anomalous coefficient. The Hall conductivity σ_{xy} values for $0.07 \leqslant x \leqslant 0.20$ taken at 14 T, i.e., presumably in the DWSM state, fairly well satisfy the relation $\sigma_{xy} \propto \sigma_{xx}^{1.6}$ (Fig. 5), which is empirically known for the intrinsic anomalous Hall effect in the large-scattering regions, e.g., $\sigma_{xy} < 10^4$ S/cm [37]. Conversely, this indicates the common origin, i.e., the anomalous Hall effect characteristic of DWSM, for the high-field σ_{xy} irrespective of the value of x or σ_{xx}. Thus we use $R_s = S_H \rho_{xx}^{0.4}$ with the scaling coefficient S_H. The solid lines in Fig. 4 are fitting curves ρ_{yx}^{fit} which reproduce ρ_{yx}^{expt} in the field-induced Gd-spin collinear region, i.e., at high magnetic fields. While the ρ_{yx}^{expt} of $x = 0.12$ is well fitted with the above relation over the entire magnetic-field range, those of other compounds in Fig. 4, which take AIAO states at zero field, show clear deviations from the fitting curves at low fields. The deviation becomes larger as temperature decreases (Fig. 10 in the Appendix). The observed ρ_{yx} should reflect the variation of the electronic states through the change of the magnetic configurations. At low fields, Ir spins form the AIAO-type magnetic ordering configuration. As the field increases, Gd spins gradually point to the field direction and force Ir spins to align in a parallel manner through the f-d exchange interaction, resulting in the breaking of the AIAO pattern accompanied by the remarkable change of ρ_{xx} and ρ_{yx} at high fields. In this regard, the origin of the deviation can be ascribed to the emergence of Weyl points (WPs) with a "distorted" AIAO magnetic state. Note here that the AIAO state maintains the cubic crystalline symmetry, and hence the net Berry curvature integrated over the Brillouin zone is canceled out in the ideal AIAO WSM. However, when the Weyl vectors connecting a pair of WPs are deformed by the Zeeman field, the Hall response can attain a considerable value, as demonstrated in $Nd_2Ir_2O_7$ under pressure [17] or epitaxially strained film [38]. Hereafter we define the deviating part

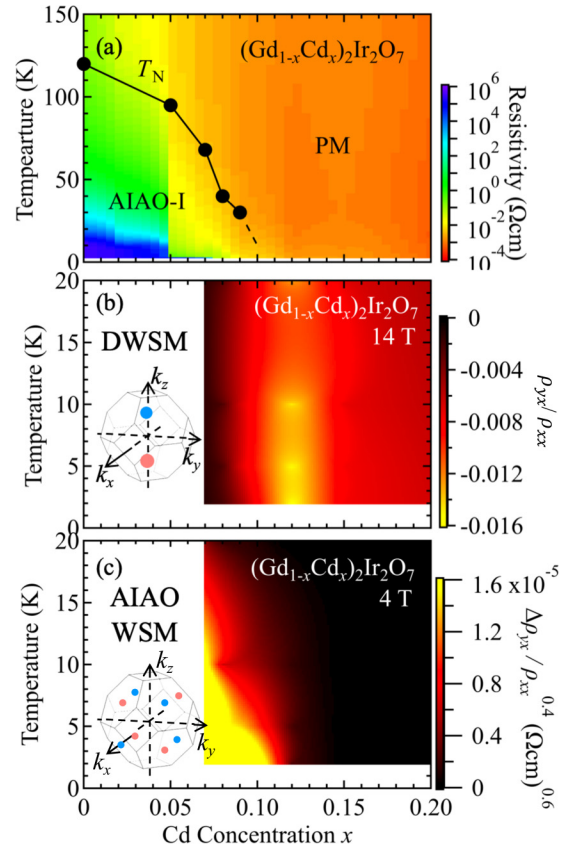

FIG. 6. (a) Phase diagram of $(Gd_{1-x}Cd_x)_2Ir_2O_7$ with contour mapping of resistivity in the plane of temperature and Cd concentration x. Black circles denote the magnetic transition temperature T_N. Also shown are contour plots of (b) the Hall angle ρ_{yx}/ρ_{xx} at 14 T and (c) $\Delta\rho_{yx}/\rho_{xx}^{0.4}$ at 4 T, which represent the Hall responses from the DWSM and AIAO WSM, respectively.

$\Delta\rho_{yx} = \rho_{yx}^{\text{expt}} - \rho_{yx}^{\text{fit}}$ as a contribution of Berry curvature in AIAO WSM.

III. DISCUSSION

To clarify the nature of the observed Hall effect in $(Gd_{1-x}Cd_x)_2Ir_2O_7$, we summarize the comprehensive results of ρ_{xx} and ρ_{yx} in contour mappings along with the phase diagram in Fig. 6. We first show the phase diagram with a contour plot of ρ_{xx} in the plane of temperature and Cd concentration x in Fig. 6(a). As x increases, T_N systematically decreases and disappears at around $x = 0.10$. Concomitantly, ρ_{xx} significantly decreases by several orders of magnitude down to approximately 1 mΩ cm in the PM phase as shown in Fig. 4(b). Figures 6(b) and 6(c) display the contour plot of the Hall angle ρ_{yx}/ρ_{xx} at 14 T and the $\Delta\rho_{yx}$ scaled with $\rho_{xx}^{0.4}$ at 4 T, which are anticipated to represent the Hall responses from the DWSM and the AIAO WSM state, respectively. Both signals are enhanced at low temperatures, suggesting that the magnetic coupling between Gd 4f and Ir 5d moments plays a vital role in the magnetotransport. As x increases, the Hall angle ρ_{yx}/ρ_{xx} at 2 K and 14 T increases steeply, reaches a maximum of 1.5% at $x = 0.12$, and mildly decreases yet sustains 0.7% at $x = 0.20$ [Fig. 6(b)], which is far beyond the value of

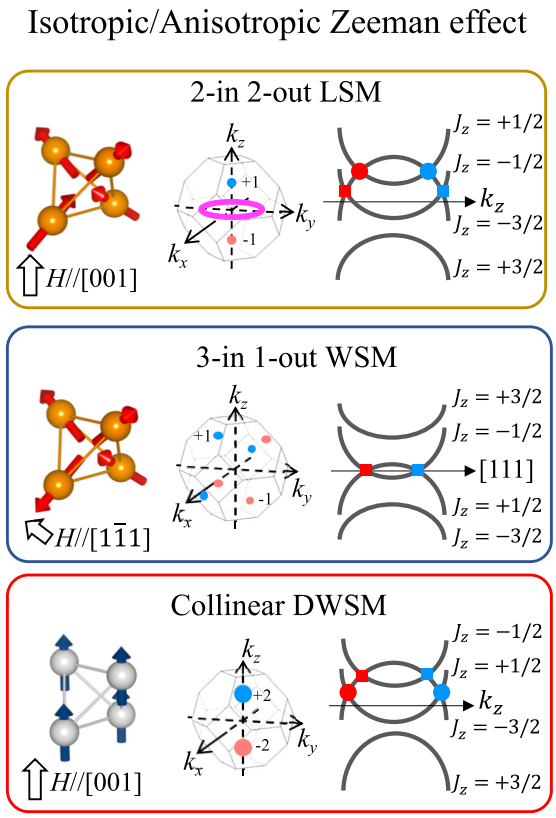

FIG. 7. Schematic picture of electronic band structures with different magnetic ordering patterns stemming from the quadratic band touching semimetal at zero magnetic field in Fig. 1(b). Shown from top to bottom are the line-node semimetal with a two-in two-out magnetic state, the Weyl semimetal with a three-in one-out magnetic state, and the double Weyl semimetal with a collinear magnetic state. Shown on the left are the respective magnetic ordering configurations. The middle column displays the distribution of Weyl points and a line node in the Brillouin zone. The red and blue circles denote Weyl points with different chiralities and the purple line denotes a line node. Shown on the right are the schematic band energy levels for respective electronic states. Red and blue squares (circles) denote Weyl points with monopole charges of ± 1 (± 2).

$(Tb_{1-x}Ca_x)_2Ir_2O_7$, which exhibits two-in two-out LSM. Such a large Hall effect is attributable to efficient Berry-curvature generation in the DWSM phase that hosts a pair of WPs with monopole charges of ± 2. In addition, it can be also augmented by the strong magnetic interaction between conducting electrons and local moments that can manifest as the upturn of ρ_{xx} (Fig. 2). On the other hand, a finite value of $\Delta\rho_{yx}/\rho_{xx}^{0.4}$ at 4 T [Fig. 6(c)] extends over the large area of the AIAO phase ($x < 0.10$). It is in sharp contrast to the AIAO WSM phase at zero field for the undoped case of $(Nd, Pr)_2Ir_2O_7$, which is constricted in the narrow temperature window, i.e., within approximately 2 K just below T_N [17]. According to theoretical calculation [35], the WPs in AIAO WSM move away from [111] or equivalent high-symmetry axes under the uniform Zeeman field which breaks threefold rotational symmetry. Consequently, the pair annihilation is prevented in the broad parameter region, leading to the expansion of the WSM phase as discussed for the case of $(Nd, Pr)_2Ir_2O_7$ [20].

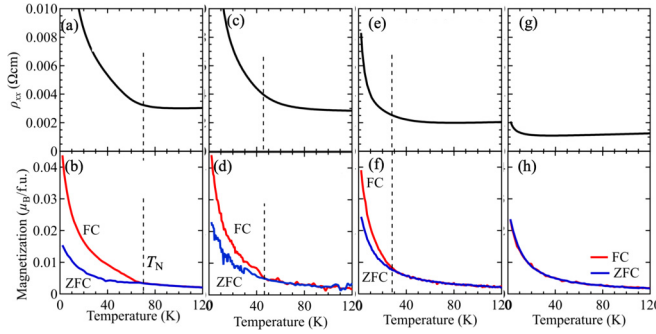

FIG. 8. Temperature dependence of (a), (c), (e), and (g) resistivity and (b), (d), (f), and (h) magnetization for $(Gd_{1-x}Cd_x)_2Ir_2O_7$. The Cd concentration is (a) and (b) $x = 0.07$, (c) and (d) $x = 0.08$, (e) and (f) $x = 0.09$, and (g) and (h) $x = 0.12$. The vertical dashed line indicates the magnetic transition temperature.

In short, as seen in Fig. 6, the compounds undergo a critical transformation from the AIAO WSM to the QBT SM at zero field as well as to the DWSM under the fully aligned Gd moments, as the hole doping proceeds across the Mott transition point ($x \sim 0.10$). Here we note that the divalent ion substitution introduces some disorder to the system and could affect the topological electronic states, although the topological system is basically robust against them. In fact, Ref. [25] demonstrates that the QBT state, which is realized in the presence of cubic symmetry, exhibit a unique Seebeck effect even in heavily doped compounds. Thus we speculate that the topological states including magnetic ones are sustained in the doped systems as well. The robustness for the topological state against chemical disorder is an interesting question and remains to be solved in a future study.

IV. SUMMARY

We investigated the magnetotransport properties in the course of hole-doping-induced Mott transitions for pyrochlore iridates R = Eu, Gd, and Tb. We established versatile phase diagrams of topological states, including the all-in all-out Weyl semimetal, the two-in two-out line-node semimetal, the quadratic-band-touching semimetal, and the double-Weyl semimetal, as functions of R ionic radius, temperature, magnetic field, and band filling (hole doping). Among them, $(Gd_{1-x}Cd_x)_2Ir_2O_7$ exhibits characteristic Hall effects which point to the different Berry-curvature generations in two distinct topological semimetals, i.e., the field-distorted all-in all-out Weyl semimetal and the double-Weyl semimetal. The present work has shown that the control of electron correlation by tuning not only the bandwidth but also the band filling can unravel the hidden topological semimetal state or dramatically expand its stable region in pyrochlore iridates where the field selection of the specific WSMs is also possible via the exchange coupling between the rare-earth $4f$ and Ir $5d$ moments.

ACKNOWLEDGMENTS

We thank Hiroaki Ishizuka for enlightening discussions. This work was supported by JSPS Grant-in-Aid for

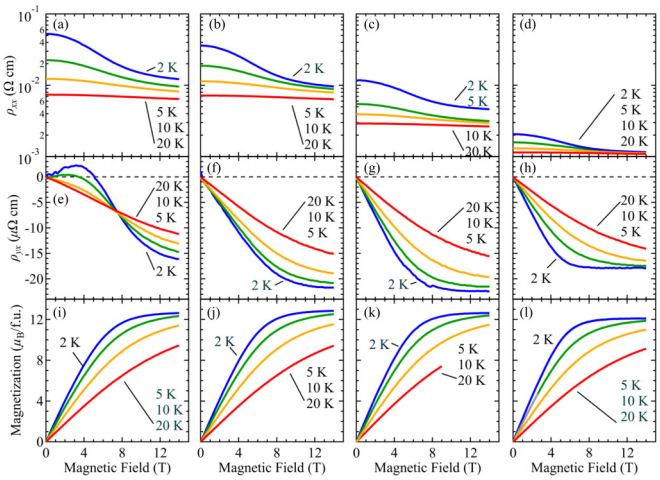

FIG. 9. Magnetic-field dependence of (a)–(d) Hall resistivity, (e)–(h) resistivity, and (i)–(l) magnetization for $(Gd_{1-x}Cd_x)_2Ir_2O_7$. The data are (a), (e), and (i) $x = 0.07$, (b), (f), and (j) $x = 0.08$, (c), (g), and (k) $x = 0.09$, and (d), (h), and (l) $x = 0.12$.

Scientific Research (No. 19K14647), and CREST (Grants No. JPMJCR16F1 and No. JPMJCR1874), Japan Science and Technology Japan.

APPENDIX

1. Possible topological semimetal states with different magnetic configurations

The electronic state of pyrochlore iridates in the paramagnetic metal phase is predicted to host a quadratic band touching at the Γ point which is actually observed by angle-resolved photoemission spectroscopy [12]. Such an electronic state is anticipated to be converted to versatile topological states by symmetry breaking, as predicted in some theories [3,14,20,35]. Figure 7 displays a representative example for the electronic band modulation with magnetic ordering patterns. In the case of a two-in two-out type of magnetic configuration, the line-node semimetal, which possesses a pair of WPs along the [001] direction and a line node in the k_z plane, can be stabilized. On the other hand, three pairs of WPs appear when the three-in one-out type of magnetic pattern is realized. Furthermore, the exchange field of collinearly aligned R spins (or extremely large Zeeman field) can give rise to the double-Weyl semimetal that host a pair of WPs with monopole charge of ±2.

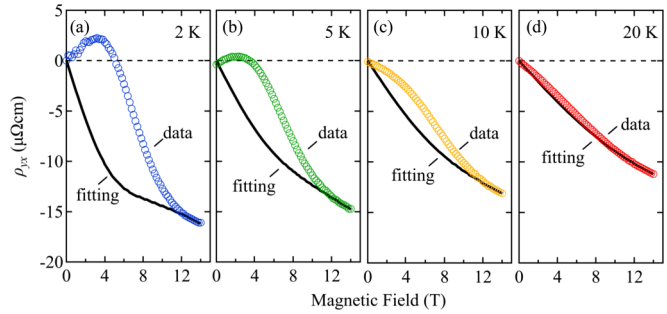

FIG. 10. Magnetic-field dependence of Hall resistivity for $(Gd_{1-x}Cd_x)_2Ir_2O_7$ ($x = 0.07$) at temperatures (a) 2 K, (b) 5 K, (c) 10 K, and (d) 20 K. Thick black lines are fitting curves (see the text).

2. Transport and magnetization properties in $(Gd_{1-x}Cd_x)_2Ir_2O_7$

Figure 8 shows the temperature dependence of resistivity and magnetization for various $(Gd_{1-x}Cd_x)_2Ir_2O_7$ compounds. For $x = 0.07$, magnetization in the field-cooling process (red lines) clearly deviates from that in the zero-field-cooling process (blue line) at the magnetic transition temperature, at which the resistivity shows a slight upturn. As x increases, the transition temperature systematically decreases while the resistivity decreases. The anomaly is no longer observed for $x = 0.12$.

3. Magnetotransport properties for hole-doped R = Gd compounds

Figure 9 shows the magnetic-field dependence of resistivity, Hall resistivity, and magnetization for various $(Gd_{1-x}Cd_x)_2Ir_2O_7$ compounds. For all compounds, the resistivity remarkably decreases with increasing field at 2 K. The reduction of resistivity becomes smaller as the temperature is elevated. Hall resistivity for $x = 0.07$ shows nonmonotonic behavior whereas the magnetization simply increases as discussed in the main text. Figure 10 shows the magnetic-field dependence of experimentally obtained Hall resistivity (circles) and the fitting curve (solid lines). The deviation of the data from the fitting curve is explicit at 2 K. This behavior fades out as temperature and x increase. For $x = 0.12$, which is paramagnetic metal down to 2 K, the Hall resistivity seems to be proportional to the magnetization in the whole temperature and magnetic-field region, as shown in Fig. 9.

[1] N. P. Armitage, E. J. Mele, and V. Ashvin, Rev. Mod. Phys. **90**, 015001 (2018).
[2] Y. Tokura, K. Yasuda, and A. Tsukazaki, Nat. Rev. Phys. **1**, 126 (2019).
[3] X. Wan, A. M. Turner, A. Vishwanath, and S. Y. Savrasov, Phys. Rev. B **83**, 205101 (2011).
[4] A. A Zyuzin and A. A. Burkov, Phys. Rev. B **86**, 115133 (2012).
[5] N. Nagaosa, J. Sinova, S. Onoda, A. H. MacDonald, and N. P. Ong, Rev. Mod. Phys. **82**, 1539 (2010).
[6] S. Nakatsuji, N. Kiyohara, and T. Higo, Nature (London) **527**, 212 (2015).
[7] T. Suzuki, R. Chisnell, A. Devarakonda, Y.-T. Liu, W. Feng, D. Xiao, J. W. Lynn, and J. G. Checkelsky, Nat. Phys. **12**, 1119 (2016).
[8] E. Liu *et al.*, Nat. Phys. **14**, 1125 (2018).
[9] N. J. Ghimire, A. S. Botana, J. S. Jiang, J. Zhang, Y.-S. Chen, and J. F. Mitchell, Nat. Commun. **9**, 3280 (2018).
[10] M. Imada, A. Fujimori, and Y. Tokura, Rev. Mod. Phys. **70**, 1039 (1998).

[11] J. S. Gardner, M. J. P. Gingras, and J. E. Greedan, Rev. Mod. Phys. **82**, 53 (2010).
[12] T. Kondo *et al.*, Nat. Commun. **6**, 10042 (2015).
[13] J. Cano, B. Bradlyn, Z. Wang, M. Hirschberger, N. P. Ong, and B. A. Bernevig, Phys. Rev. B **95**, 161306(R) (2017).
[14] E.-G. Moon, C. Xu, Y.-B. Kim, and L. Balents, Phys. Rev. Lett. **111**, 206401 (2013).
[15] W. Witczak-Krempa and Y. B. Kim, Phys. Rev. B **85**, 045124 (2012).
[16] Y. Machida, S. Nakatsuji, S. Onoda, T. Tayama, and T. Sakakibara, Nature (London) **463**, 2120 (2010).
[17] K. Ueda, R. Kaneko, H. Ishizuka, J. Fujioka, N. Nagaosa, and Y. Tokura, Nat. Commun. **9**, 3032 (2018).
[18] K. Ueda, J. Fujioka, B.-J. Yang, J. Shiogai, A. Tsukazaki, S. Nakamura, S. Awaji, N. Nagaosa, and Y. Tokura, Phys. Rev. Lett. **115**, 056402 (2015).
[19] Z. Tian, Y. Kohama, T. Tomita, H. Ishizuka, T. H. Hsieh, J. J. Ishikawa, K. Kindo, L. Balents, and S. Nakatsuji, Nat. Phys. **12**, 134 (2016).
[20] K. Ueda, T. Oh, B.-J. Yang, R. Kaneko, J. Fujioka, N. Nagaosa, and Y. Tokura, Nat. Commun. **8**, 15515 (2017).
[21] K. Ueda, J. Fujioka, Y. Takahashi, T. Suzuki, S. Ishiwata, Y. Taguchi, M. Kawasaki, and Y. Tokura, Phys. Rev. B **89**, 075127 (2014).
[22] E. Y. Ma, Y.-T. Cui, K. Ueda, S. Tang, K. Chen, N. Tamura, P. M. Wu, J. Fujioka, Y. Tokura, and Z.-X. Shen, Science **350**, 538 (2015).
[23] K. Ueda, J. Fujioka, and Y. Tokura, Phys. Rev. B **93**, 245120 (2016).
[24] H. Fukazawa and Y. Maeno, J. Phys. Soc. Jpn. **71**, 2578 (2002).
[25] R. Kaneko, M.-T. Huebsch, S. Sakai, R. Arita, H. Shinaoka, K. Ueda, Y. Tokura, and J. Fujioka, Phys. Rev. B **99**, 161104(R) (2019).
[26] W. K. Zhu, M. Wang, B. Seradjeh, F. Yang, and S. X. Zhang, Phys. Rev. B **90**, 054419 (2014).
[27] Z. Porter, E. Zoghlin, S. Britner, S. Husremovic, J. P. C. Ruff, Y. Choi, D. Haskel, G. Laurita, and S. D. Wilson, Phys. Rev. B **100**, 054409 (2019).
[28] K. Ueda, J. Fujioka, Y. Takahashi, T. Suzuki, S. Ishiwata, Y. Taguchi, and Y. Tokura, Phys. Rev. Lett. **109**, 136402 (2012).
[29] F. F. Tafti, J. J. Ishikawa, A. McCollam, S. Nakatsuji, and S. R. Julian, Phys. Rev. B **85**, 205104 (2012).
[30] M. Udagawa, H. Ishizuka, and Y. Motome, Phys. Rev. Lett **108**, 066406 (2012).
[31] Z. Wang, K. Barros, G.-W. Chern, D. L. Maslov, and C. D. Batista, Phys. Rev. Lett **117**, 206601 (2016).
[32] Z. Fang, N. Nagaosa, K. S. Takahashi, A. Asamitsu, R. Mathieu, T. Ogasawara, H. Yamada, M. Kawasaki, Y. Tokura, and K. Terakura, Science **302**, 92 (2003).
[33] T. Miyasato, N. Abe, T. Fujii, A. Asamitsu, S. Onoda, Y. Onose, N. Nagaosa, and Y. Tokura, Phys. Rev. Lett. **99**, 086602 (2007).
[34] S. Iguchi, N. Hanasaki, and Y. Tokura, Phys. Rev. Lett. **99**, 077202 (2007).
[35] T. Oh, H. Ishizuka, and B.-J. Yang, Phys. Rev. B **98**, 144409 (2018).
[36] H. Guo, K. Matsuhira, I. Kawasaki, M. Wakeshima, Y. Hinatsu, I. Watanabe, and Z.-A. Xu, Phys. Rev. B **88**, 060411(R) (2013).
[37] S. Onoda, N. Sugimoto, and N. Nagaosa, Phys. Rev. B **77**, 165103 (2008).
[38] W. J. Kim, T. Oh, J. Song, E. K. Ko, Y. Li, J. Mun, B. Kim, J. Son, Z. Yang, Y. Kohama, M. Kim, B.-J. Yang, and T. W. Noh, Sci. Adv. **6**, eabb1539 (2020).